Processing and Application of Ceramics 13 [4] (2019) 376–386
https://doi.org/10.2298/PAC1904376A

Role of interfacial charge transfer process in the graphene-ZnO-MoO_3 core-shell nanoassemblies for efficient disinfection of industrial effluents

Rajendran Ajay Rakkesh[1,2], Dhinasekaran Durgalakshmi[3], Ponnuraj Karthe[2], Subramanian Balakumar[1,*]

[1]*National Centre for Nanoscience and Nanotechnology, University of Madras, Chennai - 600 025, India*
[2]*CAS in Crystallography and Biophysics, University of Madras, Chennai - 600 025, India*
[3]*Department of Medical Physics, Anna University, Chennai - 600 025, India*

Received 26 June 2019; Received in revised form 9 October 2019; Accepted 17 November 2019

Abstract

A combined wet chemical strategy was adopted to fabricate size controllable ZnO-MoO_3 core-shell nanostructures by varying the surface potential in the reaction medium. The layered MoO_3 was adsorbed on the surface of ZnO particles by electrostatic interaction and simultaneously anchored onto graphene nanosheets (GNS) by chemical bonds. The sunlight induced photocatalytic phenomena of the GNS-ZnO-MoO_3 hybrid nanoassemblies have been examined by photodegradation of harmful organic pollutant. As a result, the as-synthesized GNS-ZnO-MoO_3 hybrid nanoassemblies showed a better photocatalytic performance towards acridine orange dye (AO). The efficient photocatalytic performance was due to the interfacial charge transfer processes between GNS and ZnO-MoO_3 that improves the electronic conductivity of the hybrid nanostructure. Moreover, the chemical bonds formed between the MoO_3 shells and GNS efficiently hinder the recombination loss of photogenerated charges. This synthesis strategy was very simple, effective and can be extended to assembling other ternary nanostructures with enhanced photodegradation performance.

Keywords: *core-shell GNS-ZnO-MoO_3, nanoassemblies, interfacial charge transfer, photocatalytic activity*

I. Introduction

Incredible efforts have been developed towards the examination of novel and effective photocatalytic materials to enhance the efficacy of solar energy conversion and environmental cleaning application. With a wide band gap energy of ~3.37 eV, ZnO has become a well-known photocatalyst among all metal oxides because of its high surface area and high photosensitivity [1,2]. Unfortunately, the photocatalytic activity of the pure ZnO is constrained by its low efficiency due to the rapid recombination rate of photo-generated electron and hole pairs [3]. The tailoring of the morphology and chemical composition, especially surface modification, play a vital role in the enhancement of the photocatalytic activity [4–6]. Modifying ZnO with inorganic semiconductor, such as MoO_3 (co-catalysts) to form a core-shell like assembly which works as an electron trapping agent, can improve its photocatalytic activity by separation of electrons and holes via the formation of heterojunction between semiconductor-semiconductor interfaces [7–11].

The photocatalytic efficiency of the core-shell nanostructures should be increased if a graphene nanosheet (GNS) is introduced into the hybrid system [12–14]. Recently, GNS has been receiving great interest in the photocatalytic field due to its large specific surface area, better electrical conductivity and excellent physiochemical properties [15,16]. Moreover, GNS darkens the hybrid material that extends their absorption range to almost the entire visible-light spectrum [17–19].

Two major concerns have to be noted for the rational design and fabrication of GNS incorporated core-shell hybrid nanostructures: i) control of particulate size and ii) interface between the co-catalyst and GNS. One of the most capable strategies to control the ZnO nanomaterial size is to restrict the nanomaterial growth within individual MoO_3 shells and then incorporate the core-

* Corresponding author: tel: +91 44 2220 2749,
e-mail: *balasuga@yahoo.com*

shells onto the GNS surfaces by chemical bonding [20–22]. This hybrid nanostructure could be used as a high-performance photocatalytic material. However, the fabrication of GNS-ZnO-MoO_3 core-shell nanostructures by wet chemical method is difficult because of the complex assembly and chemical bonding with graphene nanosheets.

In this work, a combined wet chemical method was used for the fabrication of size-controlled ZnO-MoO_3 core-shell structures incorporated onto graphene nanosheets (Fig. 1). By using this method, the size of ZnO nanoparticles can be controlled from ~20 nm to ~25 nm by simply changing the reaction temperature. MoO_3 layers formed on the surface of ZnO result in electrostatic attraction due to the variation in the surface potential between ZnO-MoO_3 core-shell structures which are engineered homogeneously onto GNS by chemical interaction with the shell layer. This hybrid nanostructure exhibited an enhanced photocatalytic performance in the degradation of organic harmful contaminants under sunlight irradiation.

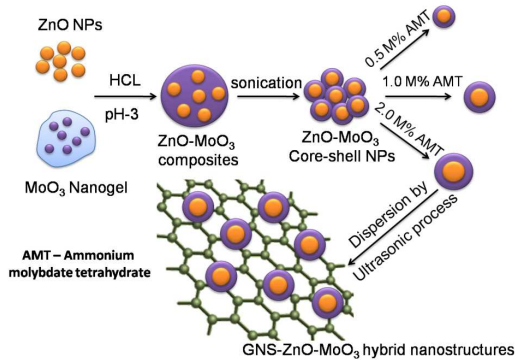

Figure 1. Schematically represented the synthesis procedure of GNS-ZnO-MoO_3 hybrid nanoassemblies by wet chemical techniques

II. Experimental

2.1. Materials

Analytical grade chemicals were used in this work without any additional purification: graphite (325 mesh, Alfa Aesar), potassium permanganate (Sigma-Aldrich), sulfuric acid, hydrochloric acid, (Rankem Chemicals), hydrogen peroxide (30 wt.%, Sigma-Aldrich), zinc acetate dihydrate (Fischer Chemicals), oxalic acid (Fischer Chemicals), ammonium molybdate tetrahydrate (Alfa Aesar), ethanol (Hayman limited) and acridine orange dye (Fischer Chemicals).

2.2. Synthesis of ZnO nanoparticles

Zinc acetate dihydrate ($Zn(CH_3COO)_2 \cdot 2\,H_2O$) was dissolved in 200 ml double-distilled water under vigorous stirring for few minutes at ~5 °C to form solution with concentration of 1.0 mol%. Oxalic acid ($H_2C_2O_4 \cdot 2\,H_2O$), dissolved in 200 ml double-distilled water at ~5 °C with concentration of 1.5 mol%, was slowly added to the cooled zinc acetate solution. It was stirred for 2 h continuously at low temperature and the solution was gradually turned to white precipitate. The precipitate was then filtered and washed with ethanol and allowed to dry at 80 °C for 2 h and that ended up in zinc oxalate formation. The zinc oxalate was further calcined at 400 °C for 2 h to form pure ZnO nanoparticles.

2.3. Synthesis of MoO_3 nanogel

In a typical experiment, using low temperature sol-gel method, 0.50 g of ammonium molybdate tetrahydrate ($(NH_4)_6Mo_7O_{24} \cdot 4\,H_2O$) was dissolved in 2 ml of high pure ethanol and hydrolysed with 4 ml of double-distilled water in a 50 ml glass beaker covered with glass lid. The entire reaction was carried out in an ice bath for 5 h under vigorous stirring until a fluid gel was obtained.

2.4. Preparation of ZnO-MoO_3 core-shell particles

ZnO-MoO_3 core-shell nanoparticles with different MoO_3 shell thickness were prepared by combined wet chemical method. The synthesized ZnO nanoparticles were dispersed in 100 ml of distilled water by ultrasonication process. The prepared MoO_3 shell material, which is unstable in the neutral pH, was introduced in ZnO dispersion at acidic conditions. The instability of the MoO_3 nanogel was controlled by adding HCl to adjust the pH value of 3 due to changes in the surface potential of the individual nanomaterials. Further on, the surface charge difference is associated with a pH that supports the production of the uniform coating of colloidal MoO_3 layers on the ZnO surfaces. Then the suspension was aged at room temperature for 2 h and finally dried isothermally at 80 °C for 12 h. The final residue was transferred into the furnace at various 400 °C for 2 h to crystallize the nanomaterials. The thickness of the MoO_3 shell size could be varied by changing the concentration of molybdenum precursor. The following concentrations were used: 0.5, 1.0 and 2 mol% and the corresponding samples have the following notation: ZM-0.5, ZM-1 and ZM-2, respectively.

2.5. Synthesis of GNS-ZnO-MoO_3 nanostructures

The detailed synthesis procedure for GNS decoration part was reported elsewhere [10,11]. The synthesized GNS (100 mg) were dispersed in double distilled water (100 ml) using ultrasonicator to form a colloidal suspension. The GNS solution was added to a higher molybdenum concentration of ZnO-MoO_3 core-shell (ZM-2) suspension (100 mg of material is dispersed in 100 ml double distilled water). The obtained precipitate was stirred vigorously for 30 min and separated by centrifugation at 4000 rpm. The resulting product was washed with ethanol and dried in a vacuum oven at 100 °C for 24 h to get GNS-ZnO-MoO_3 hybrid nanoassemblies.

2.6. Characterizations

The zeta potential was measured by Malvern Zetasizer Nano ZS90 model with 50 mW at 532 nm

laser source. X-ray diffraction (XRD) studies were carried out using a PANalytical X-ray diffractometer using CuKα (λ = 1.54 Å) radiation. All the peaks were indexed and subsequently matched with the JSCPDS database. XPS analysis was studied using ESCA+, Omicron Nanotechnology ESCA probe spectrometer using monochromatized Al Kα X-rays (energy: 1486.6 eV). The binding energy was calibrated in respect to the adventitious C 1s feature at 284.6 eV. Using the CASA-XPS software, all the spectra were deconvoluted to their component peaks. High-resolution scanning transmission electron microscopy (HRSTEM) was used to image the as-prepared nanoassemblies using an FEI Tecnai G2 S-twin instrument with a UHR pole piece. The Perkin Elmer MPF-44B equipment was used for photoluminescence studies (PL) under 325 nm excitation.

2.7. *Photocatalytic experiments*

The photocatalytic performance of the GNS-ZnO-MoO_3 hybrid nanoassemblies was investigated with the model organic pollutant AO under natural solar light irradiation following our previous work reported elsewhere [18,19]. In this process, 50 ml of AO dye solution with different concentrations (0.03 mM, 0.035 mM and 0.04 mM) and 50 mg of the GNS-ZnO-MoO_3 nanostructures were mixed and stirred for about 1 h. Before exposing to sunlight illumination, the suspensions were stirred in the dark for 30 min to confirm the establishment of adsorption/desorption equilibrium of AO on the sample surfaces. Consequently, the suspension was exposed to direct sunlight and all the experiments were carried out under similar conditions on sunny days in Chennai city (geographical location 13.04° N and 80.17° E on the south-east coast of India), between 12:00 p.m. and 3:00 p.m. (outside temperature, 29 to 31 °C). The measured illuminance power of the sunlight at the specified time interval was about 110000 Lux to 120000 Lux that was measured using a Digital luminance meter (TES Electrical Electronic Corp. Taiwan). At a particular time gap of irradiation, 5 ml of the suspension was withdrawn and consequently, the samples were centrifuged at a rate of 3000 rpm for 5 min. UV-Vis absorption spectra of the supernatant were then taken with a Lambda 650 model Perkin Elmer UV-visible spectrophotometer at the absorption line of 491 nm. The EIS spectra were recorded at ambient condition using CH instrument, 660E model cyclic voltammetry.

III. Results and discussion

3.1. *Structure and chemical bond formations*

Surface potential was studied to investigate the core-shell formation strategy by identifying the surface charges of the as-prepared ZnO and MoO_3 nanomaterials. Figure 2 exhibits the relation between surface potential and pH of the as prepared nanomaterials suspended in an aqueous medium. The obtained potentials

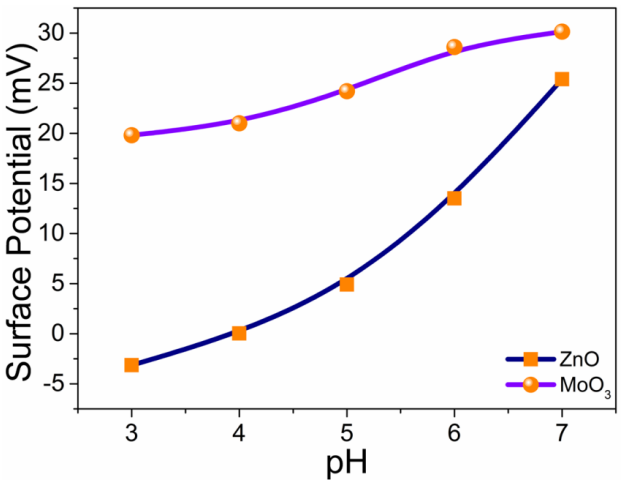

Figure 2. Zeta potential with respect to pH plot for ZnO and MoO_3 nanomaterials

were decreased with a decrease in pH, as it is an essential criterion for surface coating phenomena and also the core-shell fabrication approach. The dissimilarity in surface potential is associated with the pH variation in the materials. While reducing the pH of both pure ZnO and MoO_3 by HCl addition (to pH = 3), the surface potential values are −3.14 mV and +19.8 mV, respectively. As the MoO_3 shell nanolayer has higher surface charge compared to the core ZnO particles, the as-fabricated MoO_3 nanogel was decorated on the surface of ZnO particles by electrostatic attraction. It could be an evidence to confirm that the nanoshells have coated on the surface of ZnO particulates [23,24].

The XRD analysis was utilized to study the crystallographic phases of the as-fabricated ZnO, ZM-0.5, ZM-1 and ZM-2 core-shells and GNS-ZnO-MoO_3 hybrid nanoassemblies, as exhibited in Fig. 3. XRD pattern evidently confirms the crystalline phase of wurtzite ZnO. All diffraction peaks of the pure ZnO agreed well with the data reported in JCPDS card no. 36-1451. We observed broadening of the ZnO peaks in ZM-0.5, ZM-1 and ZM-2 core-shell structure by increasing the concen-

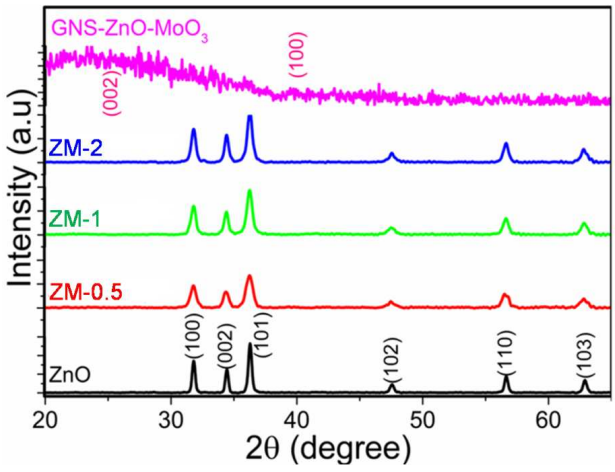

Figure 3. XRD patterns of ZnO, ZnO-MoO_3 and GNS-ZnO-MoO_3 hybrid nanoassemblies

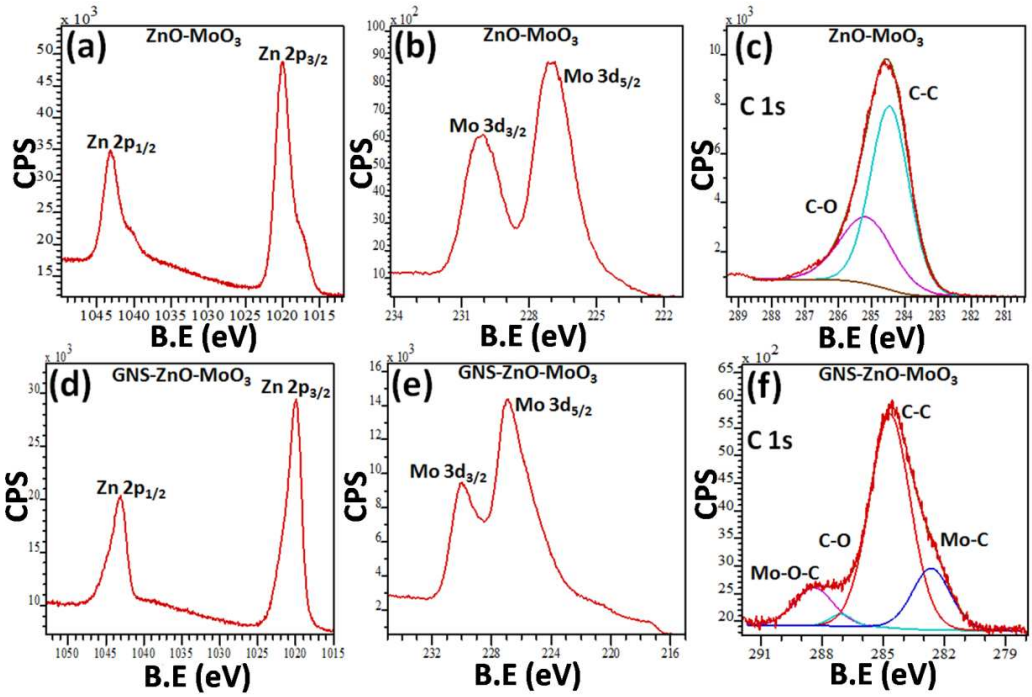

Figure 4. The Zn 2*p*, Mo 3*d* and C 1*s* XPS spectra; ZnO-MoO_3 core-shell nanomaterials (a, b and c) and GNS-ZnO-MoO_3 hybrid nanoassemblies (d, e and f)

tration of molybdenum precursors. In the GNS-ZnO-MoO_3 hybrid nanostructures, GNS presence was confirmed by the broad peaks at 25.7° and 41.16°, matching the (002) and (100) crystal planes. It is apparent that the graphene oxide is significantly reduced to nearly pure graphene nanomaterials [25,26]. Very low quantity of the ZM-2 core-shell nanostructure was chemically bonded to the surface of GNS that can be compared and confirmed with individual nanomaterials. Nevertheless, the presence of MoO_3 and the nature of bonding occuring in the synthesis reaction of ZnO-MoO_3 core-shell with GNS can be elucidated by XPS investigation, as conversed in the subsequent section.

The ZnO-MoO_3 core-shell and GNS-ZnO-MoO_3 hybrid nanoassemblies were further analysed by XPS studies. In ZnO-MoO_3 core-shell nanostructure, the peaks located at 1020.2 eV and 1043.2 eV match to Zn $2p_{3/2}$ and Zn $2p_{1/2}$, respectively, representing the existence of Zn^{2+} state (Fig. 4a). Figure 4b shows the doublet pattern arising from the spin orbit splitting of Mo 3*d* level. The binding energies are observed at 226.9 eV and 230.2 eV corresponding to Mo $3d_{5/2}$ and Mo $3d_{3/2}$ shells indicating the existence of Mo^{6+} oxidation state, respectively. The above XPS data reveal the presence of ZnO and MoO_3 in the core-shell assembly [27,28]. Further on, the deconvoluted peaks found at the binding energy of 284.6 eV and 285.6 eV were assigned to the C–C and C–O bonds (Fig. 4c) that suggests the occurrence of only a few oxygen-containing functional groups in ZnO-MoO_3 core-shell nanostructures.

Figures 4d and 4e show the high-resolution XPS spectral regions of Zn 2*p* and Mo 3*d* for GNS-ZnO-MoO_3 hybrid nanoassemblies. Figure 4d shows doublets of Zn $2p_{3/2}$ and Zn $2p_{1/2}$ found at 1020.4 eV and 1043.4 eV, respectively. The severance among these two peaks is 24.0 eV, as expected for ZnO. Figure 4e illustrates the Mo 3*d* XPS spectrum that has two bands in this region. The bands that are centred at binding energies of 226.8 eV and 231.0 eV, are assigned to the Mo $3d_{5/2}$ and Mo $3d_{3/2}$ spin orbital-splitting of photoelectrons in the Mo^{6+} oxidation state, respectively. Besides, the small shifts in the Mo 3*d* peak position were accredited to the formation of Mo–C bonding.

The C 1*s* graph of the GNS-ZnO-MoO_3 hybrid nanoassemblies (Fig. 4f) can be deconvoluted into four peaks at binding energies of 282.6 eV, 284.6 eV, 287.0 eV and 288.6 eV that are assigned to Mo–C, C–C, C–O and Mo–O–C groups, respectively. The oxygen-containing bond at 282.6 eV on the GNS surface can perform as a bonding site for MoO_3. During the synthesis process, the oxygen-containing group entirely reduced and converted to C–Mo bond which is present in the shell layer of the core-shell nanostructures. In addition, the peak at 285.6 eV disappears and shifts to 287.0 eV and a characteristic peak emerges at 288.6 eV accredited to Mo–O–C bond. This shift indicates that the –OH group of MoO_3 possibly interacts with the –COOH group on the surface of GNS during the reaction process [18,19,29].

For further understanding the bonding behaviour of the GNS-ZnO-MoO_3 hybrid nanoassemblies, the band gap of the as-fabricated ZnO, core-shells and hybrid nanoassemblies were determined from the Kubelka-Munk reflection plots drawn from the UV-visible reflectance spectra (Fig. 5). The band gaps of the materials were determined by extrapolating and intersect-

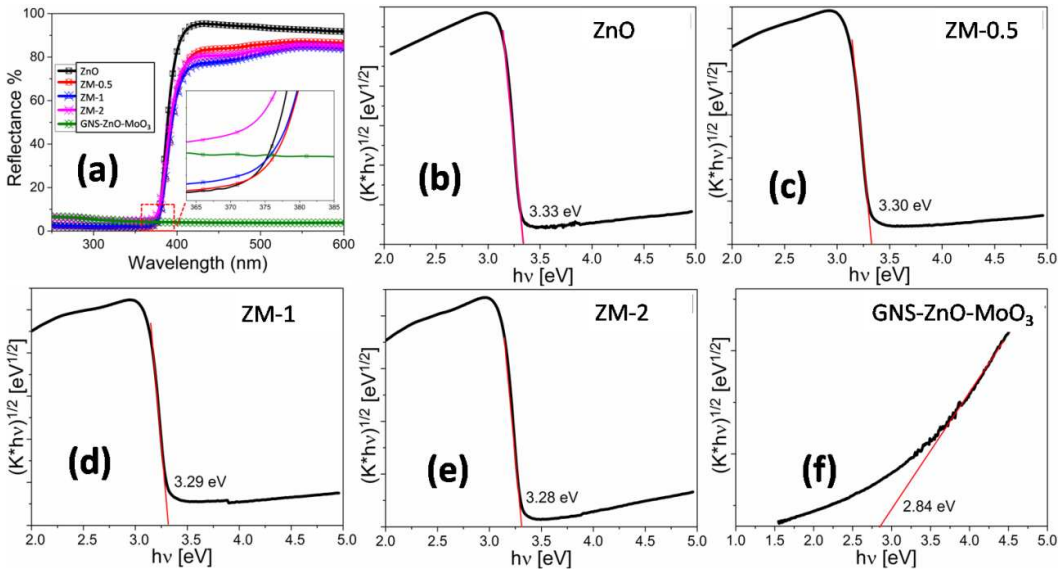

Figure 5. UV-Vis diffused reflectance spectra of ZnO, ZM-0.5, ZM-1, ZM-2 and GNS-ZnO-MoO_3 nanostructures

ing the linear portion of $(K \times h\nu)^{1/2}$ [$eV^{1/2}$] to the energy axis $h\nu$. The band gap energy values for the ZnO, ZM-0.5, ZM-1 and ZM-2 core-shells and GNS-ZnO-MoO_3 hybrid nanoassemblies were found to be 3.33, 3.30, 3.29, 3.28 and 2.84 eV, respectively. Incorporation of this core-shell nanostructure in the surface of GNS shifts the band gap energy toward the higher absorption wavelength due to the chemical bonding between C–Mo, which is in good agreement with the XPS results.

3.2. Morphological studies

The electron microscope images of the as-synthesized ZnO, MoO_3, ZM-0.5, ZM-1, and ZM-2 core-shell nanostructures and GNS-ZnO-MoO_3 hybrid nanoassemblies are shown in Figs. 6, 7 and 8. The resultant morphologies of the ZnO nanomaterials had spherical structure of diameter ranging from 20 nm to 25 nm as shown in Fig. 6a. To fabricate core-shell nanostructures, MoO_3 gel with particles of a few nanometers was coated onto the ZnO under stimulated reaction medium.

Owing to the deviation in the surface potential of the individual nanomaterials, ZnO-MoO_3 core-shell nanostructures were shaped by electrostatic attraction between the nanoparticles as shown in Figs. 7a, 7b and 7c. The outer shell thickness is in the range of ~2 to 4 nm for ZM-0.5, ~5 to 6 nm for ZM-1 and ~8 to 10 nm for ZM-2, respectively. The respective insets clearly show that the surfaces of ZnO were completely coated with crystalline MoO_3 nanoshells of different thickness obtained by increasing the concentration of molybdenum precursor.

Figure 8a exhibits formed GNS as uniformly layered and its ultra-thin wrinkled mat like structure. It is apparent that the GNS certainly served as a two-dimensional support for the integration and subsequent growth of homogeneous core-shell nanostructures. After incorporation of the ZnO-MoO_3 core-shell nanostructure with the largest shell thickness, the GNS was chemically decorated with ZnO-MoO_3 core-shell nanostructures. Due to the preferential nucleation reaction in the synthesis environment, the surface of the ZnO-MoO_3 nanostructures was chemically bonded (Figs. 8b and 8c) with

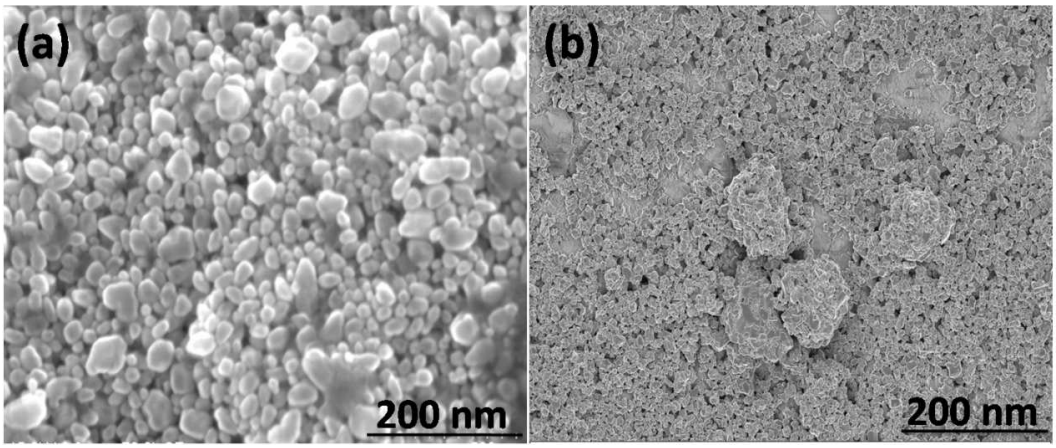

Figure 6. Electron micrographs of: a) ZnO and b) MoO_3 nanomaterials

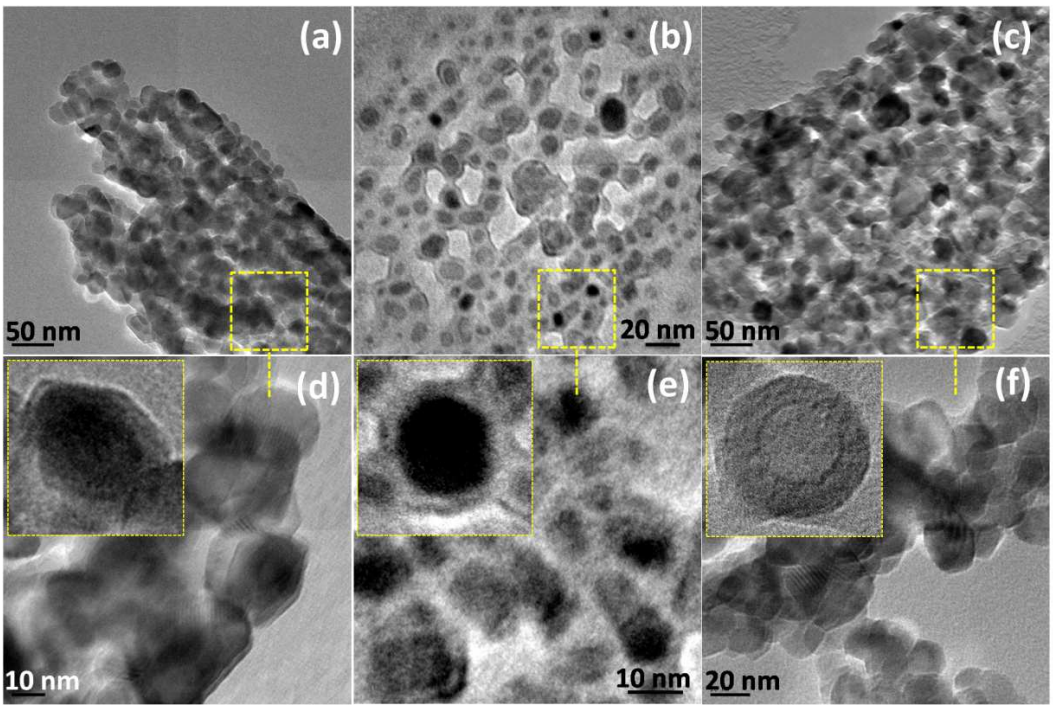

Figure 7. TEM micrographs of ZM-0.5 (a,d), ZM-1 (b,e), ZM-2 (c,f) core-shells nanostructures

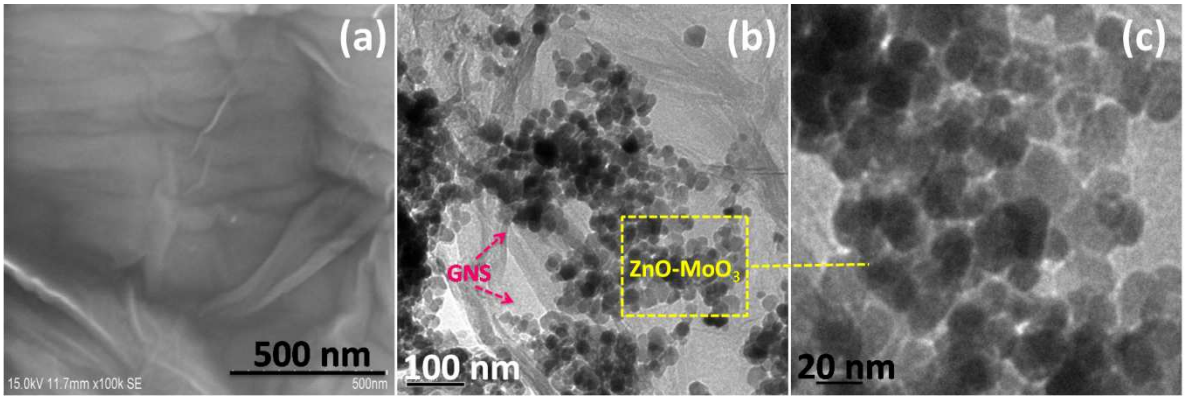

Figure 8. Electron micrographs of GNS (a), GNS-ZnO-MoO_3 (b) and magnified image of the GNS-ZnO-MoO_3 hybrid nanoassemblies

the GNS surface. The surface morphology and elemental composition studies of the GNS-ZnO-MoO_3 hybrid nanoassemblies have also been performed using FE-SEM, TEM and EDS experiments, and confirmed the presence of zinc, oxygen and molybdenum.

3.3. Photocatalytic performances and its mechanism

The photocatalytic activity of the as-fabricated ZnO, ZnO-MoO_3, and GNS-ZnO-MoO_3 hybrid nanoassemblies were investigated by observing the degradation rate of mutagenic organic pollutant (AO) in direct sunlight irradiation. The absorption spectra changes of AO aqueous solutions exhibited the concentration changes of AO. The degradation rate ($D\%$) is calculated by the mathematical equation as given below [30]:

$$D\% = \frac{C_0 - C}{C_0} \times 100\% \qquad (1)$$

where initial (C_0) and final (C) concentrations of AO are measured by UV-Vis.

Figure 9a presents the AO degradation against irradiation time plot for ZnO, ZnO-MoO_3, and GNS-ZnO-MoO_3 hybrid nanostructure photocatalysts. C/C_0 plot showed that AO dye with the 3.0×10^{-5} M concentration was decayed for about 74% with ZnO, 86% with ZM-0.5 core-shell, 92% with ZM-1 core-shell, 100% with ZM-2 core-shell all within 100 min and 100% for GNS-ZnO-MoO_3 hybrid nanostructures within only 30 min (Fig. 9b) under direct sunlight irradiation. The GNS-ZnO-MoO_3 hybrid nanoassemblies showed higher photocatalytic efficiency compared to both pure and core-shell nanostructure materials. These results certainly confirmed that GNS boosted the photocatalytic performance of ZnO-MoO_3 core-shell nanomaterial under direct sunlight irradiation.

In addition, the stability of the hybrid nanostructure

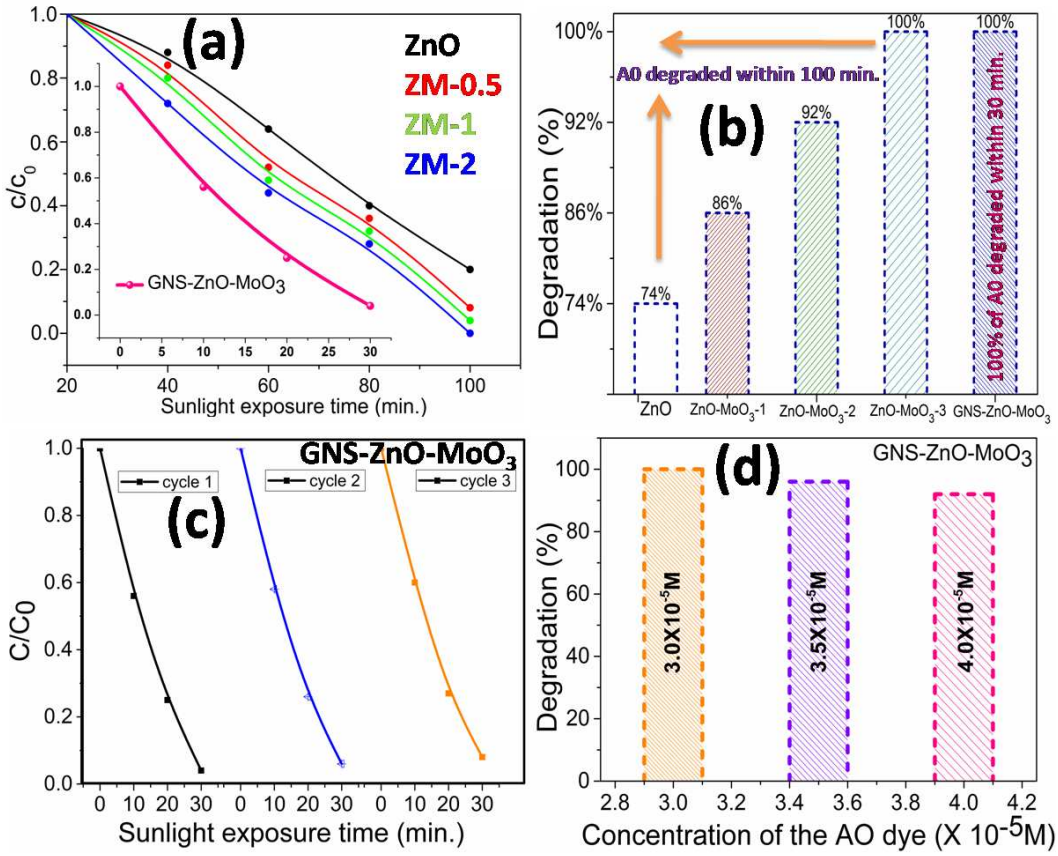

Figure 9. Time-dependent photocatalytic activity plot (a), degradation percentage of AO in the presence of as-prepared nanostructures (b), stability and reusability studies (c) and concentration dependent AO dye degradation under 30 min duration of sunlight irradiation using GNS-ZnO-MoO_3 hybrid nanoassemblies (d)

photocatalysts was studied by three experimental cycles which is essential for the photocatalyst to be proposed for use in the environmental technology. Figures 9c and 9d present that the photocatalytic degradation of AO over the GNS-ZnO-MoO_3 hybrid nanoassemblies under direct sunlight irradiation was efficient. More prominently, by changing the AO dye concentration such as 3.0×10^{-5} M, 3.5×10^{-5} M and 4.0×10^{-5} M it was exhibited that the GNS-ZnO-MoO_3 hybrid photocatalyst can easily degrade the AO dye within 30 min of irradiation in sunlight and can be separated and recycled by centrifugation. It can significantly advance their practical application to degrade and destroy the chemical chains of mutagenic organic pollutants in waste-water.

To determine the formation of reactive radicals involved in the photocatalytic activity, radicals trapping experiment has been demonstrated (Fig. 10). In a typical experimental procedure, 10 mM of Isopropyl alcohol, 10 mM of benzoquinone and 10 mM of sodium oxalate were added in the AO/photocatalyst solution to scavenge $^{\bullet}OH$, $^{\bullet}O^{2-}$ and h^+, respectively. The photodegradation efficiency of AO pollutant in the presence of above mentioned scavengers has been calculated. It is found that, the degradation efficiency was 81%, 59% and 21% in the presence of isopropyl alcohol, benzoquinone and sodium oxalate, respectively. It could be concluded that $^{\bullet}OH$ acts as a primary reactive species and $^{\bullet}O^{2-}$ as a secondary reactive species in the efficient photodegradation process.

From the above results, the proposed mechanism of the efficient photocatalytic performance towards the degradation of harmful organic pollutants under sunlight can be credited mainly to chemically bonded interface structure between GNS and MoO_3 shell in ZnO-MoO_3 core-shell nanostructures. During the photocatalytic process, the conduction as well as valence band

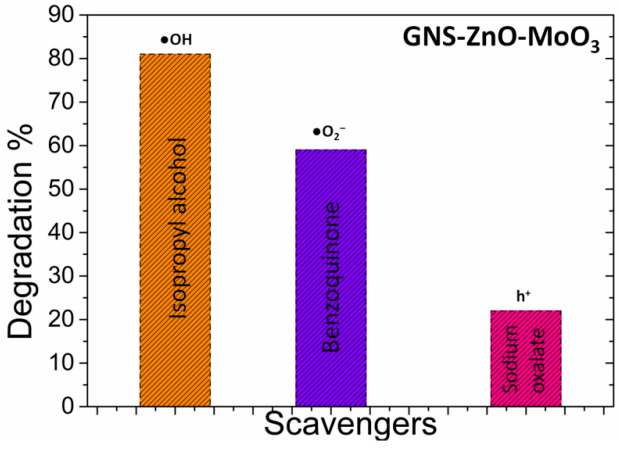

Figure 10. Reactive species involved in the photodegradation process of AO using GNS-ZnO-MoO_3 hybrid nanostructures under sunlight irradiation

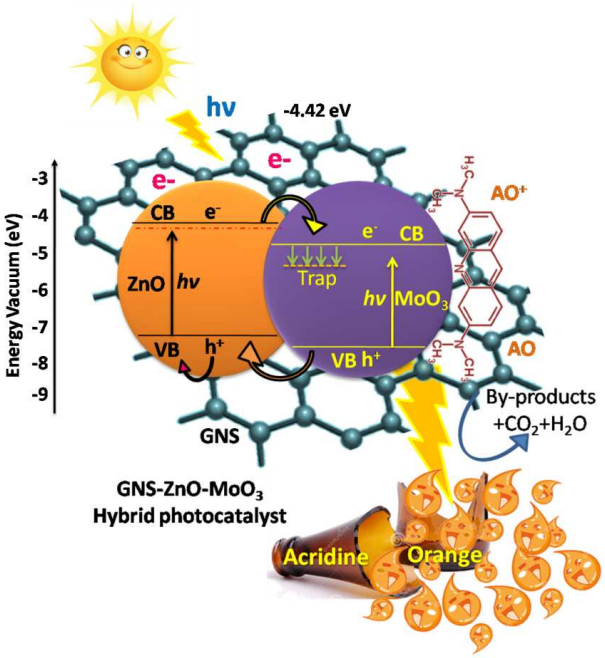

Figure 11. Schematic representation of the charge transfer process involved in GNS-ZnO-MoO_3 hybrid nanoassemblies

of ZnO lies above the energy band of MoO_3. It means that the photoinduced electrons can transfer from ZnO to MoO_3, which is due to the alignment of energy band levels at the interface of the ZnO-MoO_3 core-shell heterojunction. The positive holes created in MoO_3 can migrate to the valence band of ZnO nanomaterial and thereafter might be trapped on the surface. Thus, the photogenerated electrons and holes can be separated more efficiently at the interface of the ZnO-MoO_3 core-shell. However, the oxygen molecules adsorbed on the surface of the photocatalysts would react with the free electrons. Moreover, during the transfer of these free electrons from one semiconductor grain to another they should get through the potential barrier which limits the electron mobility. If the semiconductor nanostructures were bonded chemically to the GNS surface, they can be able to decrease the potential barrier. These chemical bonding perhaps provides a capability of transporting charge carriers and offers superior spatial conditions between semiconducting nanostructures and GNS by means of interface structures [31–33].

In contrast, photogenerated electrons could not flow directly from AO to ZnO-MoO_3 core-shell nanostructures (Fig. 11), as there was a mismatch in their energy levels. The photogenerated electron from AO flows into conduction band (CB) of MoO_3 shell in the ZnO-MoO_3 nanostructures through GNS and consequently radical species are generated. Generally, pollutants are aromatic compounds that produce π–π stacking with GNS. Subsequently, photocatalyst degrade the pollutants by the formation of oxidants and reduction of radicals [34–36]. As a result, the photodegradation is improved by chemical bonding of the core-shell nanostructures with the surfaces of GNS. Furthermore, the influence of interface engineering could improve the photocatalytic performance of the hybrid GNS-ZnO-MoO_3 nanoassemblies.

3.4. Interfacial charge transfer and recombination analysis

The efficient photodegradation performance of the GNS-ZnO-MoO_3 is attributed to the interfacial charge transfer process, which rapidly enhances the number of holes involved in the process of photo-oxidation and

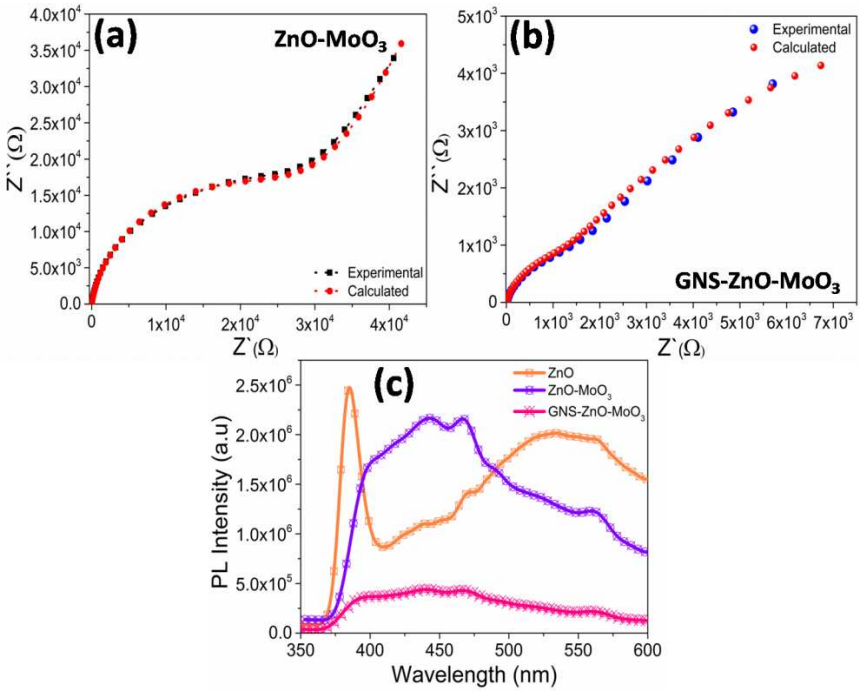

Figure 12. EIS and photoluminescence spectra of: a) ZnO, b) ZnO-MoO_3 and c) GNS-ZnO-MoO_3 hybrid nanoassemblies

effectively hinders the recombination rate of electron-hole pairs. The interfacial charge transfer process is experimentally determined by EIS and PL spectroscopic studies. Figures 12a and 12b show the EIS Nyquist plots of the ZnO-MoO_3 and GNS-ZnO-MoO_3 hybrid nanoassemblies, respectively. The radius of the EIS Nyquist curve for the GNS-ZnO-MoO_3 is smaller than for the ZnO-MoO_3 nanostructure. The smaller semicircle is a proof of a rapid interfacial charge transfer and also effective charge separation capability. The rate of recombination of photogenerated electron-hole pair is a significant factor, which affects the light induced catalytic performance of a photocatalyst. The recombination rate of electron-hole pair can be experimentally found by room temperature PL emission spectra. Decrease of the PL emission intensity indicates the enhanced charge separation efficacy. Figure 12c presents the PL emission spectra of ZnO, ZnO-MoO_3, and GNS-ZnO-MoO_3 hybrid nanoassemblies. It is evident that the UV peaks with significant intensity at 385 nm and the feeble green emission peak at 535 nm were obtained for the ZnO nanomaterials owing to its free excitonic emission and localized defect states, respectively [16,19]. The PL spectra of the ZnO-MoO_3 core-shell nanostructure as compared to the ZnO nanomaterials show that the intensity of the ZnO peaks decreased and shifted significantly owing to the presence of MoO_3 shell layer. It is evident that the formation of heterojunction between the semiconductors undoubtedly reduces the defect all through core-shell creation process.

For evaluation, the GNS-ZnO-MoO_3 hybrid nanoassemblies were investigated with PL emission spectra. The emission intensity reduced significantly, implying that the chemical bonding with GNS can quench the fluorescence from the semiconductor nanomaterials [37–39]. This could be due to the interfacial charge transfers between the semiconductors and GNS owing to chemical bonding. Therefore, GNS is an excellent nanomaterial to enhance the photocatalytic activity by increasing the electron-hole pair lifetime that inhibits the recombination rate of electron-hole pair and accelerates the interfacial charge transfer process.

IV. Conclusions

GNS-ZnO-MoO_3 hybrid nanoassemblies were successfully fabricated by combined wet chemical techniques. Such hybrid nanoassemblies were made up of ZnO-MoO_3 core-shell nanostructure incorporated onto the GNS with interfacial contacts. The study shows that the MoO_3 shells in the ZnO-MoO_3 core-shell nanostructure are chemically bonded with the GNS confirmed by the Mo–C bond formation using XPS. The GNS-ZnO-MoO_3 nanoassemblies show evidence of higher photocatalytic performance than the pure nanomaterials. Such enhanced activity was attributed to the interfacial charge transfer processes between GNS and ZnO-MoO_3 core-shells that enhance the electronic conductivity of the hybrid nanostructure. More significantly, the chemical bonds were formed between the MoO_3 shells and GNS surface, which efficiently hinder the recombination loss of photogenerated charges.

Acknowledgement: R. Ajay Rakkesh, gratefully acknowledge the UGC, New Delhi for awarding Dr D.S. Kothari Postdoctoral fellowship (EN/16-17/0030) to support this research work.

References

1. H. Wang, S. Baek, J. Lee, S. Lim, "High photocatalytic activity of silver-loaded ZnO-SnO_2 coupled catalysts", *Chem. Eng. J.*, **146** (2009) 355–361.
2. S. Jung, K. Yong, "Fabrication of CuO-ZnO nanowires on a stainless steel mesh for highly efficient photocatalytic applications", *Chem. Commun.*, **47** (2011) 2643–2645.
3. Y. Lu, Y. Lin, D. Wang, L. Wang, T. Xie, T. Jiang, "Surface charge transfer properties of high-performance Ag-decorated ZnO photocatalysts", *J. Phys. D: Appl. Phys.*, **44** (2011) 315502; R. Ajay Rakkesh, S. Balakumar, "Strctural, electrical transport and optical stdies of Li ion doped ZnO nanostructures", *Process. Appl. Ceram.*, **8** (2014) 7–13; Y. Miao, H. Zhang, S. Yuan, Z. Jiao. X. Zhu, "Preparation of flower-like ZnO architectures assembled with nanosheets for enhanced photocatalytic activity", *J. Colloid Interf. Sci.*, **462** (2016) 9–18.
4. T. He, Y. Ma, Y.A. Cao, X.L. Hu, H.M. Liu, G.J. Zhang, W.S. Yang, J.N. Yao, "Photochromism of WO_3 colloids combined with TiO_2 nanoparticles", *J. Phys. Chem. B*, **106** (2002) 12670–12676; R. Ajay Rakkesh, S. Balakumar, "Morphology dependent photocatalytic activity of α-MoO_3 nanostructures towards mutagenic acridine orange dye", *J. Nanosci. Nanotechnol.*, **15** (2015) 4316–4324.
5. P.V. Kamat, "Photochemistry on nonreactive and reactive (semicondutor) surfaces", *Chem. Rev.*, **93** (1993) 267–300.
6. R. Ajay Rakkesh, S. Balakumar, "Facile synthesis of ZnO/TiO_2 core-shell nanostructures and their photocatalytic activities", *J. Nanosci. Nanotechnol.*, **13** (2013) 370–376; S. Balakumar, R. Ajay Rakkesh, "Core/shell nano-structuring of metal oxide semiconductors and their photocatalytic studies", *AIP Conf. Proc.*, **1512** (2013) 34.
7. V. Hasija, P. Raizada, A. Sudhaik, K. Sharma, A. Kumar, P. Singh, S.B. Jonnalagadda, V. Thakur, "Recent advances in noble metal free doped graphitic carbon nitride based nanohybrids for photocatalysis of organic contaminants in water: A review", *Appl. Mater. Today*, **15** (2019) 494–524.
8. A. Sudhaik, P. Raizada, P. Shandilya, D.Y. Jeong, J.H. Lim, P. Singh, "Review on fabrication of graphitic carbon nitride based efficient nanocomposites for photodegradation of aqueous phase organic pollutants", *J. Indust. Eng. Chem.*, **67** (2018) 28–51.
9. A. Sudhaik, P. Raizada, P. Shandilya, P. Singh, "Magnetically recoverable graphitic carbon nitride and $NiFe_2O_4$ based magnetic photocatalyst for degradation of oxytetracycline antibiotic in simulated wastewater under solar light", *J. Environm. Chem. Eng.*, **6** (2018) 3874–3883.
10. P. Raizada, A. Sudhaik, P. Singh, P. Shandilya, P. Thakur, H. Jung, "Visible light assisted photodegradation of 2,4-dinitrophenol using Ag_2CO_3 loaded phosphorus and sulphur co-doped graphitic carbon nitride nanosheets in simulated wastewater", *Arabian J. Chem.*, **13** [1] (2020) 3196–

3209.
11. S. Sharma, V. Dutta, P. Singh, P. Raizada, A.R. Sani, A.H. Bandegharaei, V. Thakur, "Carbon quantum dot supported semiconductor photocatalysts for efficient degradation of organic pollutants in water: A review", *J. Cleaner Product.*, **228** (2019) 755–769.
12. P. Shandily, D. Mittal, M. Soni, P. Raizada, A.H. Bandegharaei, A.K. Saini, P. Singh, "Fabrication of fluorine doped graphene and $SmVO_4$ based dispersed and adsorptive photocatalyst for abatement of phenolic compounds from water and bacterial disinfection", *J. Cleaner Product.*, **203** (2018) 386–399.
13. P. Shandilya, D. Mittal, A. Sudhaik, M. Soni, P. Raizada, A.K. Saini, P. Singh, "$GdVO_4$ modified fluorine doped graphene nanosheets as dispersed photocatalyst for mitigation of phenolic compounds in aqueous environment and bacterial disinfection", *Sep. Purif. Technol.*, **210** (2019) 804–816.
14. P. Shandilya, D. Mittal, M. Soni, P. Raizada, L.J. Ho, J.D. Yong, R.P. Dewedi, A.K. Saini, P. Singh, "Islanding of $EuVO_4$ on high-dispersed fluorine doped few layered graphene sheets for efficient photocatalytic mineralization of phenolic compounds and bacterial disinfection", *J. Taiwan Instit. Chem. Eng.*, **93** (2018) 528–542.
15. S. Stankovich, D.A. Dikin, G.H. Dommett, K.M. Kohlhaas, E.J. Zimney, E.A. Stach, R.D. Piner, S.T. Nguyen, R.S. Ruoff, "Graphene-based composite materials", *Nature*, **442** (2006) 282–286; A. Pavithra, R. Ajay Rakkesh, D. Durgalakshmi, S. Balakumar, "Fabricatio of high quality graphene nanosheets from camphor", *Graphene*, **2** (2014) 113–116.
16. J. Du, X. Lai, N. Yang, J. Zhai, D. Kisailus, F. Su, D. Wang, L. Jiang, "Hierarchically ordered macro-mesoporous TiO_2-graphene composite films: improved mass transfer, reduced charge recombination, and their enhanced photocatalytic activities", *ACS Nano*, **5** (2011) 590–596.
17. E. Gao, W. Wang, M. Shang, J. Xu, "Synthesis and enhanced photocatalytic performance of graphene-Bi_2WO_6 composite", *Phys. Chem. Chem. Phys.*, **13** (2011) 2887–2893.
18. R. Ajay Rakkesh, D. Durgalakshmi, S. Balakumar, "Nanostructuring of a GNS-V_2O_5-TiO_2 core-shell photocatalyst for water remediation applications under sunlight irradiation", *RSC Advances*, **5** (2015) 18633–18641; R. Ajay Rakkesh, D. Durgalakshmi, S. Balakumar, "TiO_2 impregnated graphene nanostructures: An effectual photocatalysts for water remediation application", *AIP Conf. Proc.*, **1665** (2015) 050036; R. Ajay Rakkesh, D. Durgalakshmi, S. Balakumar, "Graphene based nanoassembly for simultaneous detection and degradation of harmful organic contaminants from aqueous solution", *RSC Advances*, **6** (2016) 34342–34349.
19. R. Ajay Rakkesh, D. Durgalakshmi, S. Balakumar, "Efficient sunlight-driven photocatalytic activity of chemically bonded GNS-TiO_2 and GNS-ZnO heterostructures", *J. Mater. Chem. C*, **2** (2014) 6827–6834; H. Lv, G. Ji, Z. Yang, Y. Liu, X. Zhang, W. Liu, H. Zhang, "Enhancement photocatalytic activity of the grapite-like C_3N_4 coated hollow pencil-like ZnO", *J. Colloid Interf. Sci.*, **450** (2015), 381–387.
20. H.C. Zeng, "Ostwald ripening: A synthetic approach for hollow materials", *Curr. Nanosci.*, **3** (2007) 177–181.
21. Z. Sun, J. Guo, S. Zhu, L. Mao, J. Ma, D. Zhang, "A high-performance Bi_2WO_6-graphene photocatalyst for visible light-induced H_2 and O_2 generation", *Nanoscale*, **6** (2014) 2186–2193.
22. Q. Xiang, J. Yu, M. Jaroniec, "Graphene-based semiconductor photocatalysts", *Chem. Soc. Rev.*, **41** (2012) 782–796.
23. Y. Hu, H. Qian, Y. Liu, G. Du, F. Zhang, L. Wang, X. Hu, "A microwave-assisted rapid route to synthesize ZnO/ZnS core-shell nanostructures via controllable surface sulfidation of ZnO nanorods", *Cryst. Eng. Commun.*, **13** (2011), 3438–3443.
24. S.Y. Bae, H.W. Seo, J. Park, "Vertically aligned sulphur-doped ZnO nanowires synthesized via chemical vapour deposition", *J. Phys. Chem. B*, **108** (2004) 5206–5210.
25. D.I. Son, B.W. Kwon, D.H. Park, W.S. Seo, Y. Yi, B. Angadi, C.L. Lee, W. K. Choi, "Emissive ZnO-graphene quantum dots for white-light-emitting diodes", *Nat. Nanotech.* **7** (2012) 465–471.
26. B. Yuyu, C. Zhuoyuan, L. Weibing, H. Baorong, "Highly efficient photocatalytic performance of graphene-ZnO quasi-shell-core composite material", *ACS Appl. Mater. Interf.*, **5** (2013) 12361–12368.
27. G.N. Li, Z.L. Wang, F.L. Zheng, Y.N. Ou, Y.X. Tong, "ZnO@MoO_3 core/shell nanocables: facile electrochemical synthesis and enhanced supercapacitor performances", *J. Mater. Chem.*, **21** (2011) 4217–4221.
28. T.M. McEvoy, K.J. Stevenson, "Electrochemical preparation of molybdenum trioxide thin films: effect of sintering on electrochemical and electroinsertion properties", *Langmuir*, **19** (2003) 4316–4326.
29. J.H. Park, S. Kim, A.J. Bard, "Novel carbon-doped TiO_2 nanotube arrays with high aspect ratios for efficient solar water splitting", *Nano Lett.*, **6** (2006) 24–28.
30. S.B. Khan, M. Faisal, M.M. Rahman, A. Jamal, "Low-temperature growth of ZnO nanoparticles: photocatalyst and acetone sensor", *Talanta*, **85** (2011) 943–949.
31. H. Lu, S. Wang, L. Zhao, J. Li, B. Dong, Z. Xu, "Hierarchical ZnO microarchitectures assembled by ultrathin nanosheets: Hydrothermal synthesis and enhanced photocatalytic activity", *J. Mater. Chem.*, **21** (2011) 4228–4234.
32. N. Yang, Y. Liu, H. Wen, Z. Tang, H. Zhao, Y. Li, D. Wang, "Photocatalytic properties of graphdiyne and graphene modified TiO_2: From theory to experiment", *ACS Nano*, **7** (2013) 1504–1512.
33. H. Gao, X. Li, J, Lv, G. Liu, "Interfacial charge transfer and enhanced photocatalytic mechanism for the hybrid graphene/anatase TiO_2 (001) nanocomposites", *J. Phys. Chem. C*, **117** (2013) 16022–16027.
34. Y. Bu, Z. Chen, W. Li, B. Hou, "Highly efficient photocatalytic performance of graphene-ZnO quasi-shell-core composite material", *ACS Appl. Mater. Interf.*, **5** (2013) 12361–12368.
35. D. Chen, H. Zhang, Y. Liu, J. Li, "Graphene and its derivatives for the development of solar cells, photoelectrochemical, and photocatalytic applications", *Energy Environ. Sci.*, **6** (2013) 1362–1387.
36. N. Zhang, Y. Zhang, Y.J. Xu, "Recent progress on graphene-based photocatalysts: current status and future perspectives", *Nanoscale*, **4** (2012) 5792–5813.
37. Z. Chen, N. Zhang, Y.J. Xu, "Synthesis of graphene-ZnO nanorods nanocomposites with improved photoactivity and anti-photocorrosion", *Cryst. Eng.Commun.*, **15**

(2013) 3022–3030.
38. C. Zhang, J. Zhang, Y. Su, M. Xu, Z.Yang, Y. Zhang, "ZnO nanowire/reduced graphene oxide nanocomposites for significantly enhanced photocatalytic degradation of Rhodamine 6G", *Physica E*, **56** (2014) 251–255.
39. R. Ajay Rakkesh, D. Durgalakshmi, S. Balakumar, "Beyond chemical bonding interaction: An insight into the growth process of 1D ZnO on few-layer graphene for excellent photocatalytic and room temperature gas sensing applications", *Chem. Select*, **3** (2018) 7302–7309.